Appendix A

Theories of thin film growth

In a first approach, different morphologies of pseudomorphical films, grown by molecular beam epitaxy (MBE), can be described by minimizing the free energy [8, 168]. In *thermal equilibrium* the sum of the surface free energies of the overlayer material γ_{over}, the substrate γ_{sub}, and the free energy of the interface γ_{inter}, described by

$$\Delta\gamma = \gamma_{\text{sub}} - \gamma_{\text{over}} - \gamma_{\text{inter}} \quad , \tag{A.1}$$

leads to the three different growth modes shown in Fig. A.1:

- For $\Delta\gamma > 0$, the layer-by-layer or Frank-van der Merwe growth mode is obtained. Within this growth mode an adatom layer is completely occupied before the next layer starts to grow on top of it (Fig. A.1(a)).

- For $\Delta\gamma < 0$, the growth evolves in the three-dimensional (3D) island or Volmer-Weber growth mode (Fig. A.1(c)).

- In the intermediate layer-plus-3D-island or Stranski-Krastanov growth mode additionally, the strain due to the lattice mismatch of the overlayer and substrate material has to be considered. After an initial pseudomorphic layer-by-layer growth the film minimizes its increasing effective interface energy by forming 3D islands (Fig. A.1(b)).

The thermodynamic approach may explain the existence of the three growth modes, which are also seen in experiment, and may be useful in some cases. However, it provides only a first insight into crystal growth. For real systems it often predicts wrong morphologies, e. g. layer-by-layer growth is predicted for *homoepitaxial* films, but often different growth modes are observed for such systems. To give a further example, the free energies of the *heteroepitaxial* system Co/Cu(001) fulfil the criterion of the 3D-island growth mode ($\gamma_{\text{Cu}} = 1.85$ Jm^{-2}, $\gamma_{\text{Co}} = 2.55$ Jm^{-2}, $\gamma_{\text{CoCu}} = 0.25$ Jm^{-2} [107, 108]) but a completely different morphology is detected in experiment, as can be seen
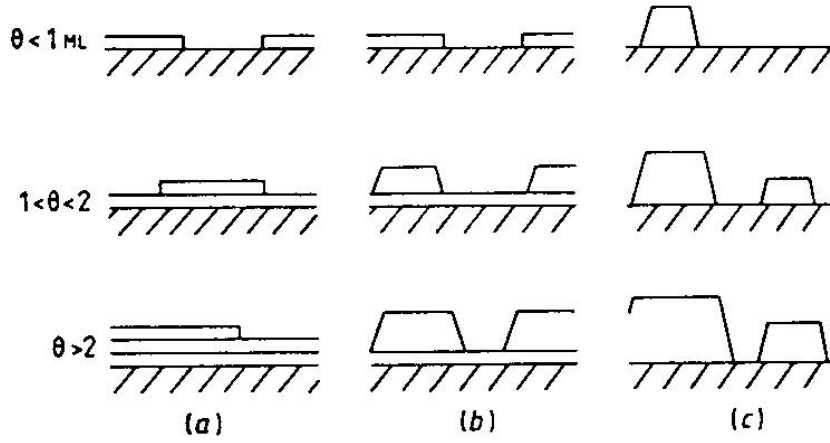
Figure A.1: Schematic representation of three crystal growth modes: (a) layer-by-layer or Frank-van der Merwe, (b) layer-plus-3D-island or Stranski-Krastanov, (c) 3D-island or Volmer-Weber growth mode. Θ represents the coverage in monolayers (ML) (taken from Ref. [168]).
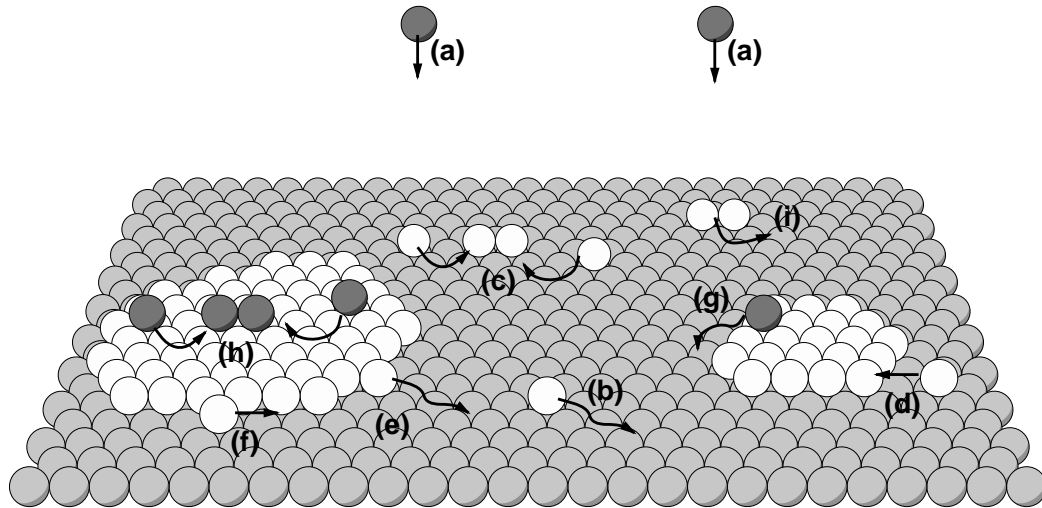

Figure A.2: Scheme of atomic processes responsible for thin film growth, see text for discussion (taken from Ref. [142]).

in Fig. 1.1, p. 15. An improved description has to take into account that MBE growth very often evolves far from thermodynamic equilibrium and results in *metastable* morphologies. This is due to the fact that crystal growth is a nonequilibrium kinetic process based on atomic processes [168, 142].

The individual atomic processes which are important for thin film growth are depicted in Fig. A.2. After deposition (a), the adatoms may diffuse over the surface (b), nucleate islands (c), be captured by islands (d), be detached from islands (e), diffuse along island edges (f), hop over island edges (g), nucleate islands on top of already existing islands (h). Even dimers and larger islands can diffuse (i). Additionally, neighbored adatoms can exchange their positions. Also an exchange with substrate atoms and desorbtion from the surface is possible (interdiffusion, not shown).

Different atomistic methods have been applied for the theoretical description of the time evolution of the surface morphology. The most important ones are shortly introduced in the following.

(1) Kinetic rate equations have been used to describe nucleation and growth of islands on the basis of atomic processes. Following Zinsmeister and Venables [180, 168, 167], the time evolution of the density of single atoms n_1 and stable islands, containing $x > 1$ atoms n_x on the substrate surface, is given by

$$\frac{dn_1}{dt} = R - \frac{n_1}{\tau_a} - \frac{d(n_x w_x)}{dt} \quad , \tag{A.2}$$

$$\frac{dn_x}{dt} = U_i - U_c - U_m \quad . \tag{A.3}$$

The deposition rate R increases the single atom density n_1, whereas the latter is reduced by the desorption term n_1/τ_a and capture by stable islands with an average number of atoms w_x per island. Assuming that all islands smaller than a critical size i are unstable, the density of stable islands n_x is increased by the rate of newly built stable clusters U_i, and is lowered due coalescence resulting from growth U_c and mobility U_m. Eqs. (A.2) and (A.3) are applicable to coverages $\Theta < 1$ ML and are often used for the interpretation of experiments. This system of coupled differential equations can be extended taking into account additional atomic processes [4, 46]. However, a derivation of a general solution is not possible due to the complexity of the problem. Thus, in different growth regimes different approximations have to be made.

(2) Molecular dynamics (MD) simulations can, in principle, treat the growth dynamics exactly [98, 59]. Here Newton's equations of motion for the atoms

$$m_i\, \boldsymbol{R}_i = -\nabla_i\, V(\{\boldsymbol{R}_i\}) \quad , \quad i = 1, \dots, N \tag{A.4}$$

are integrated numerically, $V(\{\boldsymbol{R}_i\})$ being the interatomic potential. The validity of the solutions obtained by MD calculations is limited mainly by

the 'quality' of the available interatomic potentials: the more realistic the potentials, the larger the numerical effort. In the context of film growth this method is limited by the small treatable system sizes and the short accessible time scales which are of the order of picoseconds. However, the relevant atomic processes in crystal growth are much slower than the motion of individual atoms under mutual forces. Note that the typical deposition rate of a thin film grown by MBE is of the order 1 ML/100 sec which still can be much too fast to reach equilibrium film structures. Hence, MD simulations are very useful for the study of single atomic growth mechanisms, e. g. the most probable paths in phase space and their activation energies [147, 56, 169, 103], but are not suitable for the simulation of a growing film itself.

(3) These problems are avoided within the kinetic Monte Carlo (MC) approach which is often the method of choice for the study of growing thin films. The main idea of this method is, not to calculate the dynamics on a short timescale exactly, like vibrations of an adatom at an adsorption site, but to take them into account implicitly by treating kinetics during growth as a thermally activated, stochastic process [10, 13, 92]. Then, an atomic process j (like desorption, diffusion, exchange, etc.) can be described within transition state theory [171, 172] by an Arrhenius-type rate

$$\Gamma^j = \Gamma_0^j \exp(-\Delta E^j / k_\mathrm{B} T) \quad , \tag{A.5}$$

where the prefactor Γ_0^j is the attempt frequency, ΔE^j the free energy difference between the saddle point (transition state) and the minimum (binding site) of the process, k_B the Boltzmann constant, and T the temperature [84, 50]. The kinetic MC technique solves Markov's master equation for the time evolution of the many-body system towards thermodynamical equilibrium

$$\frac{dP(\mathcal{C}, t)}{dt} = -\sum_{\mathcal{C}'} \Gamma^j(\mathcal{C} \to \mathcal{C}') \, P(\mathcal{C}, t) + \sum_{\mathcal{C}'} \Gamma^j(\mathcal{C}' \to \mathcal{C}) \, P(\mathcal{C}', t) \tag{A.6}$$

numerically where $P(\mathcal{C}, t)$ is the probability to find configuration $\mathcal{C}$ in phase space at time t. This statistical approach allows for the simulation of comparatively large systems ($\leq 1 \ \mu$m) and long time scales (1 ps $\leq t \leq$ 1 hour).

Kinetic MC simulations have been successfully applied to studies of growing semiconductors and metals [99, 102, 29, 18, 152, 83, 25, 90]. Most of these investigation are based on *simplified* models, concerning e. g. the lattice type, the restriction to one or few atomic processes, the dependence of the energy barriers on the local surroundings, or the connection of MC time to a physical time unit. A good overview of KMC applied in thin film growth is given by Levi and Kotrla in their review article [94].

Some of the state-of-the-art simulations of epitaxial growth have been realized by Scheffler and co-workers, using a so-called *ab initio* kinetic MC

method. For the system Al/Al(111) Ruggerone *et al.* calculated in a first step the energy parameters for all relevant atomic processes using density functional theory. In a second step, they included the obtained, microscopically well founded rates in a kinetic MC code [159, 138]. Recently, Pentcheva and Scheffler successfully applied the same approach to the heteroepitaxial system Co/Cu(001) which serves as the experimental model system of the present thesis, see Fig. 1.1, p. 15. The authors were able to explain the complicated initial growth behavior of Co/Cu(001) observed in experiment, like the interdiffusion of Co and Cu atoms and the bimodal growth mode. Due to the high computational cost their study is restricted to coverages up to 0.2 ML [114, 126, 125, 127].

In the present thesis, the kinetic MC method is used for the calculation of the magnetic relaxation of nanostructured films and is explained in more detail in Chapter 4.

Appendix B

Simulation of a growing fcc-(001) film

In this appendix, we demonstrate the implementation of a MC simulation of the extended Eden model on a fcc-(001) surface.

The simulation is performed on a $n \times L \times L$ fcc-(001) unit cell with L being the lateral extension in units of the interatomic distance r_o and n the number of layers. Periodic boundary conditions are applied for the calculation of the magnetic behavior of an extended film. Fig. B.1 shows schematically the top view of a fcc-(001) surface and the [100]- and [010] crystal axes. Additionally, the lattice parameter a_o and the interatomic distance $r_o = a_o/\sqrt{2}$ are sketched. For the Co/Cu(001) system, these quantities amount to $a_o = 3.5$ Å and $r_o = 2.5$ Å [124].

According to growth rule (1) of the Eden model, the simulation is initialized with an arrangement of occupied sites in the first layer which serve as island seeds for the attachment of deposited adatoms. For example, a random distribution of seeds, a regular array, or chains etc. can be applied.

In the following, we explain the method by which growth rule (2) is realized where in each growth step the probability

$$p(q, z) \propto \exp\left(-E^{\mathrm{ad}}(q, z) \,/\, k_{\mathrm{B}}\, T\right) \tag{B.1}$$

for the occupation of a perimeter site with coordination number q in layer z has to be used.

To begin with, we distinguish different types of perimeter sites which can be occupied by adatoms. In Fig. B.2, examples of the different perimeter sites, appearing for an Eden island with two layers on a fcc-(001) surface, are depicted. In the first layer $z = 1$, four different classes of perimeter sites with respective coordination numbers $q = 5, 6, 7, 8$ can be distinguished. Here, $q = 4$ resulting from possible bonds to substrate atoms only, is not allowed since adatoms must be attached to already existing islands. For
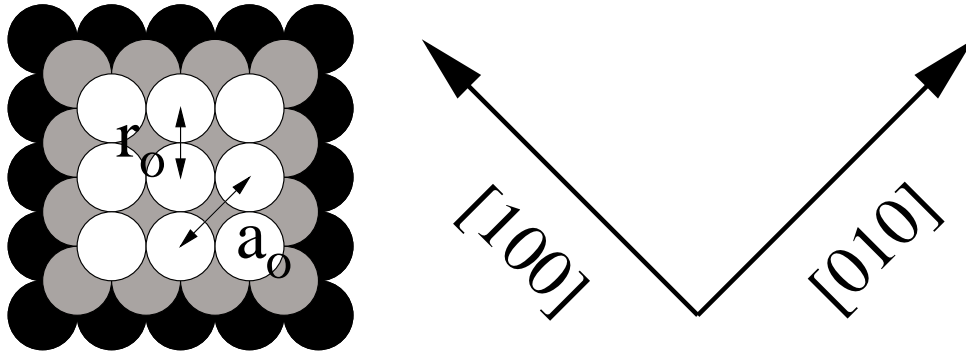
Figure B.1: Top view of a fcc-(001) surface showing three layers. For fcc-Co, as present for pseudomorphic Co/Cu(001), the lattice parameter amounts to $a_o = 3.5$ Å and the interatomic distance is given by $r_o = a_o/\sqrt{2} = 2.5$ Å [124].
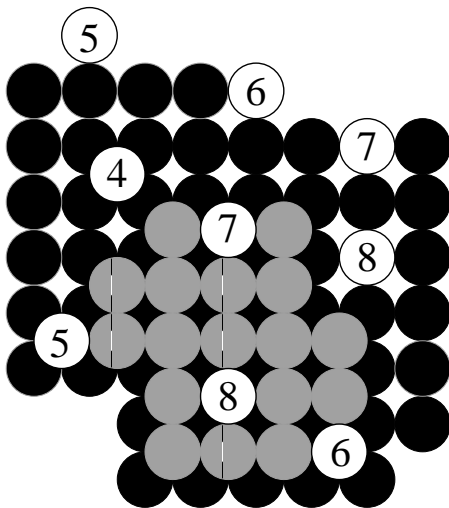

Figure B.2: A bilayer Eden island on a fcc-(001) surface is depicted, black refers to the first adatom layer $z = 1$ and grey to the second layer $z = 2$. Examples for the different classes of perimeter sites in the first layer with possible coordination numbers $q = 5, 6, 7, 8$ and in the second layer with $q = 4, 5, 6, 7, 8$ are given. The substrate surface is not shown.

Scheme of the kth growth step

generate a random number

$$r_1 \in [0, \mathcal{Q}(\mathcal{C}_k))$$

choose a particular class with q_o, z_o being the smallest numbers to fulfil

$$r_1 \leq \sum_{z=1}^{z_o} \sum_{q=4}^{q_o} \mathcal{N}_{qz} \, p(q, z)$$

choose a particular perimeter site out of the chosen class using a second random number

$$r_2 \in [0, \mathcal{N}_{q_o z_o})$$

by occupation of the chosen perimeter site the system transforms to a new configuration

$$\mathcal{C}_k \to \mathcal{C}_{k+1}$$

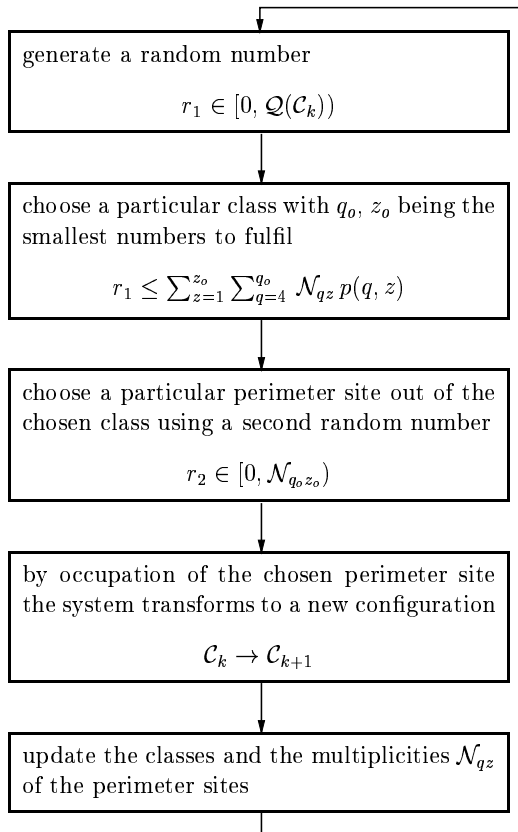update the classes and the multiplicities $\mathcal{N}_{qz}$ of the perimeter sites

Figure B.3: Schematic representation of the kth growth step describing the transition of the system from configuration $\mathcal{C}_k$ to configuration $\mathcal{C}_{k+1}$.

$z = 2$ (and for all layers $z > 2$), five different classes of perimeter sites with $q = 4, 5, 6, 7, 8$ are present. Thus, in a system with n layers there are $5n - 1$ different classes of perimeter sites, each class containing $\mathcal{N}_{qz} \geq 0$ equivalent perimeter sites with the same adatom binding energy $E^{\mathrm{ad}}(q, z)$.

We apply an algorithm where unsuccessful attempts of depositing an adatom are avoided. For this, all available classes of perimeter sites and their multiplicities $\mathcal{N}_{qz}$ have to be known in every growth step.[1] A schematic representation of the kth growth step is shown in Fig. B.3:

---

[1]This approach is similar to the so-called N-fold method which was originally formulated for MC simulations of the Ising model in order to avoid unsuccessful spin-flip attempts [16].

First, a random number r_1 is generated in the interval defined by the sum

$$\mathcal{Q}(\mathcal{C}_k) = \sum_{z=1}^{n} \sum_{q=4}^{8} \mathcal{N}_{qz}\, p(q, z) \qquad \text{(B.2)}$$

of the probabilities $p(q, z)$ and their multiplicities $\mathcal{N}_{qz}$ in the growth configuration $\mathcal{C}_k$. Then, the class of perimeter sites with $q = q_o$ and $z = z_o$ is selected in whose interval the random number falls. Hence, this class is chosen with probability $\mathcal{N}_{q_o z_o} p(q_o, z_o)/\mathcal{Q}(\mathcal{C}_k)$ as demanded by Eq. (B.1). With a second random number r_2 a particular perimeter site is selected from the list of this class which has $\mathcal{N}_{q_o z_o}$ entries. By occupying the chosen perimeter site the system transforms from the old configuration $\mathcal{C}_k$ to the new configuration $\mathcal{C}_{k+1}$. This eventually creates new perimeter sites or changes the coordination numbers of neighboring perimeter sites. Thus, the classes of available perimeter sites and their multiplicities $\mathcal{N}_{qz}$ have to be updated in the new configuration which can be done locally.

Appendix C

Hoshen-Kopelman algorithm

The Hoshen-Kopelman (HK) algorithm [68] provides an efficient method to identify clusters of neighboring occupied lattice sites (or of neighboring spins with same directions) in a single pass through the lattice. We use this method for the calculation of the percolation probability $P_L(\Theta)$ (Sec. 2.2.3) and the analysis of magnetic domains (Sec. 5.5).

In the present version for a square $L \times L$-lattice, the HK algorithm determines the entire cluster distribution, i. e. it

(i) labels lattice sites $\mathcal{L}(i,j)$, $i, j = 1, \ldots, L$, with consecutive cluster numbers $c = 1, 2, \ldots$,

(ii) counts the size of the clusters $S(c)$, and

(iii) determines the number of clusters C.

For this purpose, the scheme below is applied where we follow the description given in Ref. [146, 92]:

The lattice sites are visited in a typewriter fashion. If site (i,j) is unoccupied, it is labeled with $\mathcal{L}(i,j) = 0$ and the next site is analysed. If the lattice site (i,j) is occupied, then the following cases are distinguished:

(1) Both already visited next neighbors (NN) are unoccupied: $\mathcal{L}(i-1,j) = \mathcal{L}(i,j-1) = 0$.

— Assign the *new* cluster label $\mathcal{L}(i,j) = c$.

— The size of the new cluster amounts to $S(c) = 1$.

— Update the number of clusters, $C \to C + 1$.

(2) Exactly one NN is occupied and is labeled with c: $\mathcal{L}(i-1,j) = c$ or $\mathcal{L}(i,j-1) = c$

- Assign $\mathcal{L}(i,j) = c$.

- Increase the cluster size, $S(c) \rightarrow S(c) + 1$.

(3) Both NN are occupied and belong to the same cluster c: $\mathcal{L}(i-1,j) = \mathcal{L}(i,j-1) = c$. Proceed as in case (2).

(4) Both NN are occupied and belong to different clusters: $\mathcal{L}(i-1,j) = c$, $\mathcal{L}(i,j-1) = c'$, with $c < c'$, as an example.

- Assign the 'proper' label $\mathcal{L}(i,j) = c$.

- Combine the clusters, $S(c) \rightarrow S(c) + S(c')$.

- Register that all c'-sites now belong to cluster c by a negative 'label of the label', $S(c') = -c$.

- Update the number of clusters, $C \rightarrow C - 1$.

If a NN is analysed, check, if the cluster label is still 'valid' (positive entry $S(c)$) or if it is coupled to another cluster label (negative entry $S(c)$). If necessary, track the 'valid' cluster label and assign it to the lattice site (i,j).

Appendix D

Magnetization reversal of a single-domain particle

In this appendix, we review results on the magnetization reversal of a single-domain particle. Depending on the strength of the applied field B (reduced field $h = B/(KN)$), two cases for the reversal $\phi = 0 \rightarrow \phi = \pi$ are distinguished, see Eq. (3.11) and Fig. 3.2, p. 42: Reversal due to (1) an applied magnetic field and (2) thermal activation.

D.1 Reversal due to an external magnetic field

For magnetic fields $|B| > |B_c|$ ($|h| > 1$), no anisotropy energy barrier is present, and the particle magnetization is immediately reversed. Such a switching is dominated by *spin precession* processes. Using the assumption of coherently rotating atomic magnetic moments, Stoner and Wohlfarth (SW) were able to explain the relatively large coercive fields B_c observed experimentally for small particle ensembles [157].

Recently, Hinzke *et al.* confirmed this approach theoretically for the switching of small Co nanoparticles ($d = 5$ nm) in a reversing external field [64, 66]. For the motion of the interacting *atomic* magnetic moments $\boldsymbol{\mu}_{\mathrm{at}}$ the authors integrated the corresponding Landau-Lifshitz-Gilbert (LLG) equation with Langevin dynamics numerically. This equation of motion for a magnetic moment $\boldsymbol{S}_i = \boldsymbol{\mu}_i/\mu_i$ subject to the total effective magnetic field $\boldsymbol{H}_i = \zeta_i(t) - \partial\mathcal{H}/\partial\boldsymbol{S}_i$ denotes

$$\hbar\left(1 + \alpha^2\right)\frac{\partial\boldsymbol{S}_i}{\partial t} = -\boldsymbol{S}_i \times \left(\boldsymbol{H}_i + \alpha\left(\boldsymbol{S}_i \times \boldsymbol{H}_i\right)\right) \quad, \tag{D.1}$$

where $\hbar$ is Planck's constant and α the damping constant, which phenomenologically describes the coupling to a heat bath. Thermal fluctuations are taken into account by the time-dependent noise $\zeta_i(t)$ with $\langle\zeta_i(t)\rangle = 0$. The

first right-hand term of the LLG equation describes the precession of the magnetic moment in the effective field and can be derived from the Heisenberg equation of motion for quantum spins

$$i\hbar \frac{\partial \langle \tilde{\boldsymbol{s}}(t) \rangle}{\partial t} = \langle [\tilde{\boldsymbol{s}}(t), \tilde{\mathcal{H}}] \rangle \quad . \tag{D.2}$$

The second term is a phenomenological expression for the damping. In the low damping limit and for low temperatures, Hinzke *et al.* showed that the magnetization reversal happens via *coherent rotation* of the atomic moments as assumed in the SW model. Furthermore, the authors demonstrated that the order of magnitude of the switching time τ of the particle is given by the spin precession time of a single atomic moment $\boldsymbol{\mu}_{\mathrm{at}}$ in the external magnetic field $\boldsymbol{B}$, described by Eq. (3.12)

D.2 Thermally activated reversal over an energy barrier

For magnetic fields $|B| < |B_{\mathrm{c}}|$ ($|h| < 1$), the particle magnetization has to surmount the anisotropy energy barrier during rotation ΔE given by Eq. (3.13). This can occur via thermal activation.

Néel applied the SW model of coherent rotation to such a thermally assisted magnetization reversal and proposed for the mean switching time τ the Arrhenius-type law given by Eq. (3.14) [112]. For the prefactor τ_o, he assumed the precession time $\tau_{\mathrm{pr}}^{\mathrm{c}}$ of an *atomic* magnetic moment μ_{at} in the coercive field B_{c} (Eq. (3.12)) which is typically of the order $10^{-10} - 10^{-9}$ sec.

Brown rigorously recalculated Néels phenomenological ansatz, using the LLG equation with Langevin dynamics given by Eq. (D.1) for the motion of a single SW magnetic moment $\boldsymbol{\mu} = N\boldsymbol{\mu}_{\mathrm{at}}$ [20, 21]. He solved the corresponding Fokker-Planck equation for the evolution of the probability density of orientations for an ensemble of identical particles, and adapted Kramer's treatment of the escape of particles over energy barriers. As a result, in the limit of $KN \gtrsim k_{\mathrm{B}}T$ he was able to reproduce Néels activation law, Eq. (3.14), which is therefore usually called Néel-Brown model. Moreover, Brown estimated the prefactor τ_o in the limit $\Delta E \gg k_{\mathrm{B}}T$ to be

$$\tau_o = \frac{\pi\hbar(1+\alpha^2)}{\mu B_{\mathrm{c}}} \sqrt{\frac{k_{\mathrm{B}}T}{KN(1-h)^2}} \frac{1}{1-h^2}$$

$$= \frac{\tau_{\mathrm{pr}}^{\mathrm{c}}}{2} \frac{1}{\alpha} \sqrt{\frac{k_{\mathrm{B}}T}{\Delta E}} \frac{1}{1-h^2} \quad , \tag{D.3}$$

where $\tau_{\mathrm{pr}}^{\mathrm{c}}$ is the precession time of the moment μ in the coercive field B_{c}. Thus, the order of magnitude of τ_o is mainly determined by $\tau_{\mathrm{pr}}^{\mathrm{c}}$.

Again, Hinzke *et al.* tested the Néel-Brown model for thermal magnetization reversal numerically [65, 64, 66]. For the motion of interacting *atomic* magnetic moments $\boldsymbol{\mu}_{\text{at}}$ they used Eq. (D.1) as well as MC simulations with time step quantification. Application of this MC method yields the same results as the use of the LLG equation of motion (D.1), however, the former method is much more efficient for large time scales $\tau \gg \tau_{\text{pr}}$ [117, 116]. For spin chains (with lengths $L = 30$) and small Co particles ($d = 4$ nm), the authors found a coherent rotation mode of the moments and obtained excellent agreement with the Néel-Brown model for the characteristic time τ. For large system sizes and high temperatures, the thermally assisted magnetization reversal happens via nucleation of a domain wall, multidroplet nucleation or the so-called 'curling' mode. These reversal modes can also be described by Arrhenius-type laws using different prefactors τ_o and activation energies ΔE [64, 116].

In experiments on the thermal switching of *individual* Co nanoparticles ($d = 25$ nm) at very low temperatures ($0.1 - 6$ K) using a SQUID detector, Wernsdorfer *et al.* recently found good agreement with the Néel-Brown model and a prefactor τ_o of the order 10^{-9} sec [173, 30].

Appendix E

Ewald summation of the dipole term

In the present thesis, the lattice sums

$$\mathcal{T}_1 = \sum_j \frac{x_{ij}^2}{r_{ij}^5} \quad , \quad \mathcal{T}_2 = \sum_j \frac{y_{ij}^2}{r_{ij}^5} \quad , \quad \mathcal{T}_3 = \sum_j \frac{x_{ij}\,y_{ij}}{r_{ij}^5} \quad , \tag{E.1}$$

which appear in the dipole fields, given by Eqs. (3.26), (3.28), (3.29), (F.15), and (F.16), are performed over all islands $j \neq i$ of the unit cell and furthermore over all islands of the infinite periodic arrangement of the unit cell without using a cut-off radius. Correspondingly, the cluster dipole fields, described by Eqs. (3.46) and (3.45), are obtained by summing over all spins l outside the spin cluster, including the infinite periodical arrangement of the unit cell. A sketch of the infinite periodical arrangement of the unit cell is depicted in Fig. E.1. In the following, we discuss the summation for a single island pair and omit the island indices i, j.

The evaluation of the dipole lattice sums follows the description given by Jensen in Ref. [76]. The main idea of this method is to transform slowly converging direct lattice sums into rapidly converging ones, using Poisson's summation formula. The most general lattice sum on a 2D rectangular lattice which can be handled by Jensen's method, is given by

$$\mathcal{T}(\alpha, \beta, \gamma, \vec{q}_\parallel, z, \delta x, \delta y) = \sum_{\eta, \xi = -\infty}^{+\infty} {}' \frac{x_\eta^\beta\, y_\xi^\gamma}{r^{2\alpha}} \, \exp(iq_x x_o \eta) \, \exp(iq_y y_o \xi) \quad , \tag{E.2}$$

denoting

$$x_\eta = x_o(\eta + \delta x) \quad , \quad \delta x = \frac{\Delta x}{x_o} \quad , \quad \eta \in \mathbb{Z}_0 \quad , \tag{E.3}$$

$$y_\xi = y_o(\xi + \delta y) \quad , \quad \delta y = \frac{\Delta y}{y_o} \quad , \quad \xi \in \mathbb{Z}_0 \quad . \tag{E.4}$$
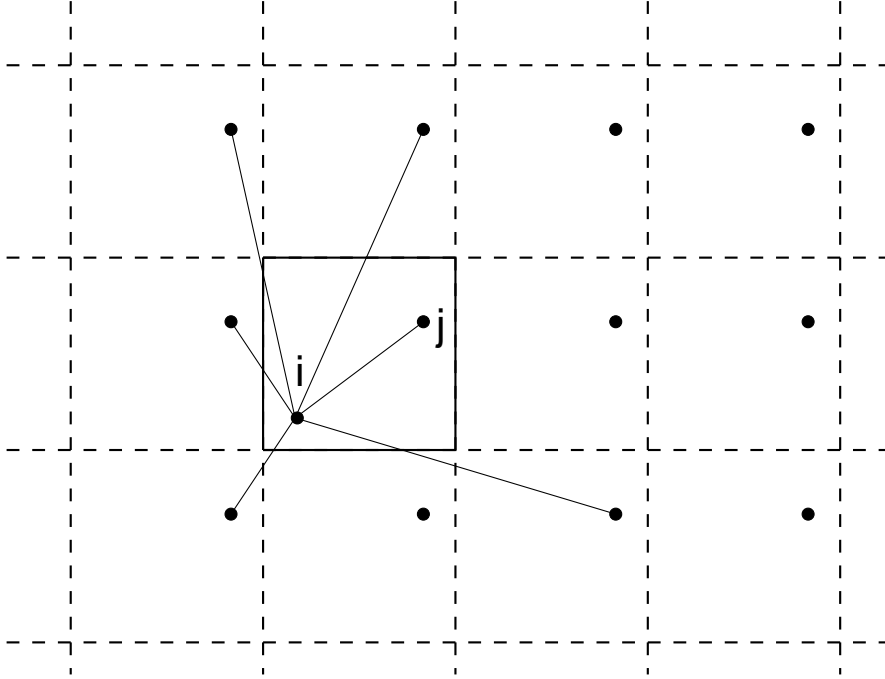
127

Figure E.1: Sketch of the infinite periodical arrangement of the unit cell. Few terms contributing to the infinite lattice sums of the island pair (i, j) are indicated by lines.

The quantities x_o and y_o are the lattice periods of the rectangular lattice, Δx and Δy refer to the lattice offsets relative to the origin ($|\Delta x| < x_o$, $|\Delta y| < y_o$). In addition, the relative lattice offsets δx and δy are defined ($\delta x < 1$, $\delta y < 1$). The distance of the lattice site (η, ξ) from the origin is given by

$$r = \sqrt{x_\eta^2 + y_\xi^2 + z^2} \quad . \tag{E.5}$$

The vertical distance of the lattice plane from the origin is given by z. The prime at the sum of Eq. (E.2) indicates that the summation term refering to $r = 0$ (appearing for $\delta x = \delta y = 0$, $\eta = \xi = 0$, and $z = 0$) has to be excluded. The numbers 2α, β, and γ ($2\alpha > \beta + \gamma$) are positive integers or zero and indicate different types of couplings. The vector $\vec{q}_\parallel$ is the 2D wave vector and q_x, q_y are the wave numbers ($|q_x| \leq \pi/x_o$, $|q_y| \leq \pi/y_o$).

The lattice sum $\mathcal{T}$ of Eq. (E.2) can be written as a derivative from a more general lattice sum

$$
\begin{aligned}
\mathcal{T}(\alpha, \beta, \gamma, \vec{q}_\parallel, z, \delta x, \delta y) \;=\;& \exp(iq_x x_o \delta x + iq_y y_o \delta y) \\
& \times \frac{\partial^\beta}{\partial(iq_x)^\beta} \frac{\partial^\gamma}{\partial(iq_y)^\gamma} \mathcal{S}(\alpha, \vec{q}_\parallel, z, \delta x, \delta y) \;, \tag{E.6}
\end{aligned}
$$

where the expression

$$
\mathcal{S}(\alpha, \vec{q}_\parallel, z, \delta x, \delta y) = \sum_{\eta, \xi = -\infty}^{+\infty} {}' \, r^{-2\alpha} \, \exp(iq_x x_\eta) \, \exp(iq_y y_\xi) \qquad \text{(E.7)}
$$

is the generating lattice sum. Jensen showed in the mentioned publication that for summations in the *same* layer, i. e. for $z = 0$, the generating direct lattice sum $\mathcal{S}(\alpha, \vec{q}_\parallel, 0, \delta x, \delta y)$ can be rewritten as the much faster converging sum

$$
\begin{aligned}
\mathcal{S}(\alpha, \vec{q}_\parallel, 0, \delta x, \delta y) = {} & \frac{2\sqrt{\pi}}{\Gamma(\alpha)} \frac{x_o^{1/2-\alpha}}{y_o} \sum_{\eta=-\infty}^{+\infty} {}' \, \exp\left(iq_x x_o(\eta - \delta x)\right) \\
& \times \sum_{\xi=-\infty}^{+\infty} \exp(-2\pi i \xi \delta y) \left(\frac{|u_\xi(q_y)|}{|\eta - \delta x|}\right)^{\alpha - 1/2} \mathcal{K}_{\alpha - 1/2}\left(2x_o|u_\xi(q_y)||\eta - \delta x|\right) \\
& + \delta_{\delta x} \sum_{\eta=-\infty}^{+\infty} {}' \, \frac{\exp\left(iq_y y_o(\eta - \delta y)\right)}{y_o^{2\alpha}(\eta - \delta y)^{2\alpha}} \quad ,
\end{aligned} \qquad \text{(E.8)}
$$

using $u_\xi(q_y) = \pi \xi / y_o + q_y/2$, the Gamma function $\Gamma(\alpha)$, and the notation

$$
\delta_{\delta x} = \begin{cases} 1 & \delta x \neq 0 \\ 0 & \delta x = 0 \end{cases} \quad . \qquad \text{(E.9)}
$$

$\mathcal{K}_\nu(x)$ is the modified Bessel function of second kind of order ν which decays *exponentially* for large arguments x and leads to the fast convergence of the new series over η and ξ.

For the dipole fields needed in the present study, the number $\alpha = 5/2$ has to be applied to Eq. (E.8). After the determination of the derivatives according to Eq. (E.6), using $\beta, \gamma = 0$ to 2, the wave numbers $q_x = q_y = 0$ have to be inserted for the summation of the *uniform* infinite arrangement of the unit cell with periodicity $x_o = y_o = L$.

Following this scheme, we obtain from Eq. (E.8)

$$
\begin{aligned}
\mathcal{S}(5/2, \vec{q}_\parallel, 0, \delta x, \delta y) = {} & \frac{8}{3x_o^2 y_o} \sum_{\eta=-\infty}^{+\infty} {}' \, \exp\left(iq_x x_o(\eta - \delta x)\right) \sum_{\xi=-\infty}^{+\infty} \exp(-2\pi i \xi \delta y) \\
& \times \left(\frac{|u_\xi(q_y)|}{|\eta - \delta x|}\right)^2 \mathcal{K}_2(2x_o |u_\xi(q_y)| |\eta - \delta x|) \\
& + \delta_{\delta x} \sum_{\eta=-\infty}^{+\infty} {}' \, \frac{\exp\left(iq_y y_o(\eta - \delta y)\right)}{y_o^5(\eta - \delta y)^5} \qquad \text{(E.10)}
\end{aligned}
$$

and in the next step

$$\frac{\partial^2}{\partial(iq_x)^2}\,\mathcal{S}(5/2,\vec{q}_\parallel,0,\delta x,\delta y) = \frac{8}{3y_o}\sum_{\eta=-\infty}^{+\infty}{}' \exp\Big(iq_x x_o(\eta-\delta x)\Big)$$

$$\times \sum_{\xi=-\infty}^{+\infty}\exp(-2\pi i\xi\delta y)\,u_\xi^2(q_y)\,\mathcal{K}_2(2x_o|u_\xi(q_y)||\eta-\delta x|) \quad . \quad (E.11)$$

Inserting the wave numbers $q_x = q_y = 0$, we yield from Eqs. (E.6) and (E.11)

$$\mathcal{T}(2,0,\delta x,\delta y) = \frac{8}{3y_o}\sum_{\eta=-\infty}^{+\infty}{}'\sum_{\xi=-\infty}^{+\infty}\exp(-2\pi i\xi\delta y)\left(\frac{\pi\xi}{y_o}\right)^2\mathcal{K}_2(2x_o|\frac{\pi\xi}{y_o}||\eta-\delta x|),$$

$$(E.12)$$

and finally, after a few transformations, the more convenient expression

$$\mathcal{T}(2,0,\delta x,\delta y) = \frac{4}{3x_o^2 y_o}\left[\frac{\delta_{\delta x}}{(\delta x)^2}+\sum_{\eta=1}^{\infty}\left(\frac{2\left(\eta^2+(\delta x)^2\right)}{(\eta^2-(\delta x)^2)^2}\right)\right]$$

$$+\frac{16\pi^2}{3y_o^3}\sum_{\xi=1}^{\infty}\xi^2\cos(2\pi\xi\delta y)\left[\delta_{\delta x}\,\mathcal{K}_2(2\pi\xi\,\delta x\,x_o/y_o)\right.$$

$$+\sum_{\eta=1}^{\infty}\Big(\mathcal{K}_2(2\pi\xi(\eta-\delta x)\,x_o/y_o)+\mathcal{K}_2(2\pi\xi(\eta+\delta x)\,x_o/y_o)\Big)\bigg].(E.13)$$

The sum $\mathcal{T}(0,2,\delta y,\delta x)$ can be calculated by usage of Eq. (E.13) and exchanging $\delta x \leftrightarrow \delta y$ and $x_o \leftrightarrow y_o$.

For the evaluation of the sum $\mathcal{T}(1,1,\delta x,\delta y)$, we proceed correspondingly from

$$\frac{\partial}{\partial(iq_y)}\frac{\partial}{\partial(iq_x)}\,\mathcal{S}(5/2,\vec{q}_\parallel,0,\delta x,\delta y) = \frac{8}{3x_o y_o}\sum_{\eta=-\infty}^{+\infty}{}'\frac{\exp\Big(iq_x x_o(\eta-\delta x)\Big)}{\eta-\delta x}$$

$$\times \sum_{\xi=-\infty}^{+\infty}\exp(-2\pi i\xi\delta y)$$

$$\times\Big(-u_\xi\,|u_\xi|\,\mathcal{K}_1(2\pi|\xi||\eta-\delta x|\,x_o/y_o)\,x_o|\eta-\delta x|\Big), \quad (E.14)$$

and obtain after setting $q_x = q_y = 0$

$$\mathcal{T}(1,1,\delta x,\delta y) = \frac{-8}{3x_o y_o i}\sum_{\eta=-\infty}^{+\infty}{}'\frac{1}{\eta-\delta x}\sum_{\xi=-\infty}^{+\infty}\exp(2\pi i\xi\delta y)$$

$$\times\left(\frac{\pi^2}{y_o^2}\,\xi\,|\xi|\,x_o|\eta-\delta x|\,\mathcal{K}_1(2\pi|\xi||\eta-\delta x|\,x_o/y_o)\right) \quad . \quad (E.15)$$

130

Finally, this lattice sum can be transformed to

$$\mathcal{T}(1,1,\delta x, \delta y) = \frac{16\pi^2}{3y_o^3} \sum_{\xi=1}^{\infty} \xi^2 \, \sin(2\pi\xi\delta y) \left[\delta_{\delta x} \, \mathcal{K}_1(2\pi\xi\delta x \, x_o/y_o) \right.$$

$$\left. - \sum_{\eta=1}^{\infty} \Big(\mathcal{K}_1(2\pi\xi(\eta - \delta x) \, x_o/y_o) - \mathcal{K}_1(2\pi\xi(\eta + \delta x) \, x_o/y_o) \Big) \right] . (E.16)$$

The dipole sums $\mathcal{T}(2,0,\delta x_{ij}, \delta y_{ij})$, $\mathcal{T}(0,2,\delta y_{ij}, \delta x_{ij})$ and $\mathcal{T}(1,1,\delta x_{ij}, \delta y_{ij})$ are now evaluated numerically for all island pairs (i,j) using Eqs. (E.13) and (E.16) .

Appendix F

Mean-field theory of magnetic order

In this appendix, we present simple mean-field theories (MFT) for the magnetic ordering. First, a MFT is given for the *internal* magnetic order within a single island. Next, a MFT is formulated for the *long-range* magnetic order of the interacting island system.

F.1 Internal island magnetic order

The coverage and temperature dependence of the *internal* island magnetization $m_i(\Theta, T)$ is described within a simple MFT as a first approximation. As a consequence, also the effective anisotropy coefficients $K_i(\Theta, T)$ and domain wall energy densities $\gamma_{ij}(\Theta, T)$ vary.

First, we treat the atomic magnetic moments as *quantum* spins $\hat{\boldsymbol{s}}$ characterized by a spin quantum number S. Within MFT the relative internal island magnetization $m_i(\Theta, T) = \langle \hat{s}^z \rangle_i / S$ is given by the Brillouin function [110]

$$
\begin{aligned}
m_i(\Theta, T) &= \mathcal{B}_S\left(x_i\right) \\[2mm]
&= \frac{2S+1}{2S} \coth\left(\frac{2S+1}{2S} x_i\right) - \frac{1}{2S} \coth\left(\frac{x_i}{2S}\right) \quad, \quad \text{(F.1)} \\[2mm]
x_i &= \frac{\overline{q}_i(\Theta)\, J\, S^2}{k_\mathrm{B}\, T}\, m_i(\Theta, T) \quad. \quad \text{(F.2)}
\end{aligned}
$$

The finite size of the island in contrast to a bulk system is considered by the average coordination number $\overline{q}_i(\Theta)$ of island i, which depends on the coverage Θ of the growing thin film. We evaluate $\overline{q}_i(\Theta)$ numerically during the growth procedure. The MFT for quantum spins leads to internal island

Curie temperatures[1] given by

$$T_{\mathrm{C}}^i(\Theta) = \frac{\overline{q}_i(\Theta)\, J\, S(S+1)}{3\, k_{\mathrm{B}}} \quad .$$ (F.3)

Alternatively, for *classical* spins $\boldsymbol{s}$ with unit length $|\boldsymbol{s}| = 1$, we can apply the Langevin function [110]

$$m_i(\Theta, T) = \mathcal{L}(x_i) = \coth x_i - \frac{1}{x_i} \quad ,$$ (F.4)

using Eq. (F.2) for $S = 1$. Here, the internal Curie temperature of the islands is given by

$$T_{\mathrm{C}}^i(\Theta) = \frac{2\, \overline{q}_i(\Theta)\, J}{3\, k_{\mathrm{B}}} \quad .$$ (F.5)

The equations (F.1) and (F.4) can be solved numerically by a simple iterative method, as explained in the next section.

The ability of the anisotropy to maintain a certain direction of the island magnetization decreases due to thermal agitation. Thus, a decreasing internal order $m_i(\Theta, T)$ causes also a decreasing effective anisotropy $K_i(\Theta, T)$. Within a first order thermodynamic pertubation theory, the anisotropy $K_i(\Theta, T)$ is given by [109]

$$K_i(\Theta, T) = K \cdot f_i(\Theta, T) \quad ,$$ (F.6)

where we use for *quantum* spins $\hat{\boldsymbol{s}}$

$$f_i(\Theta, T) = \frac{3\, \langle (\hat{s}^z)^2 \rangle_i - S(S+1)}{2S(S - \frac{1}{2})} \quad , \quad S \geq 1$$ (F.7)

and

$$\langle (\hat{s}^z)^2 \rangle_i = S(S+1) + \left(\frac{1}{2} \coth \frac{x_i}{2} - (S+\frac{1}{2}) \coth \left((S+\frac{1}{2})\, x_i \right) \right) \coth \frac{x_i}{2} \quad .$$ (F.8)

For *classical* spins $\boldsymbol{s}$, $|\boldsymbol{s}| = 1$, we apply [77]

$$f_i(\Theta, T) = \frac{3\, \langle (s^z)^2 \rangle_i - 1}{2} \quad , \quad \langle (s^z)^2 \rangle_i = 1 - \frac{2}{x_i} \coth x_i + \frac{2}{x_i^2} \quad ,$$ (F.9)

which reduces to the simple formula

$$f_i(\Theta, T) = 1 - \frac{T}{T_{\mathrm{C}}^i(\Theta)}$$ (F.10)

---

[1] The critical temperature T_{C}^i of island i is an artefact of MFT. In reality, there is no phase transition in a finite system, rather a maximum of the susceptibility χ is present instead of a singularity. For an increasing size of the island, the maximum of χ at T_{C}^i becomes rather sharp and MFT yields a simple estimate of $m_i(T)$ [174].
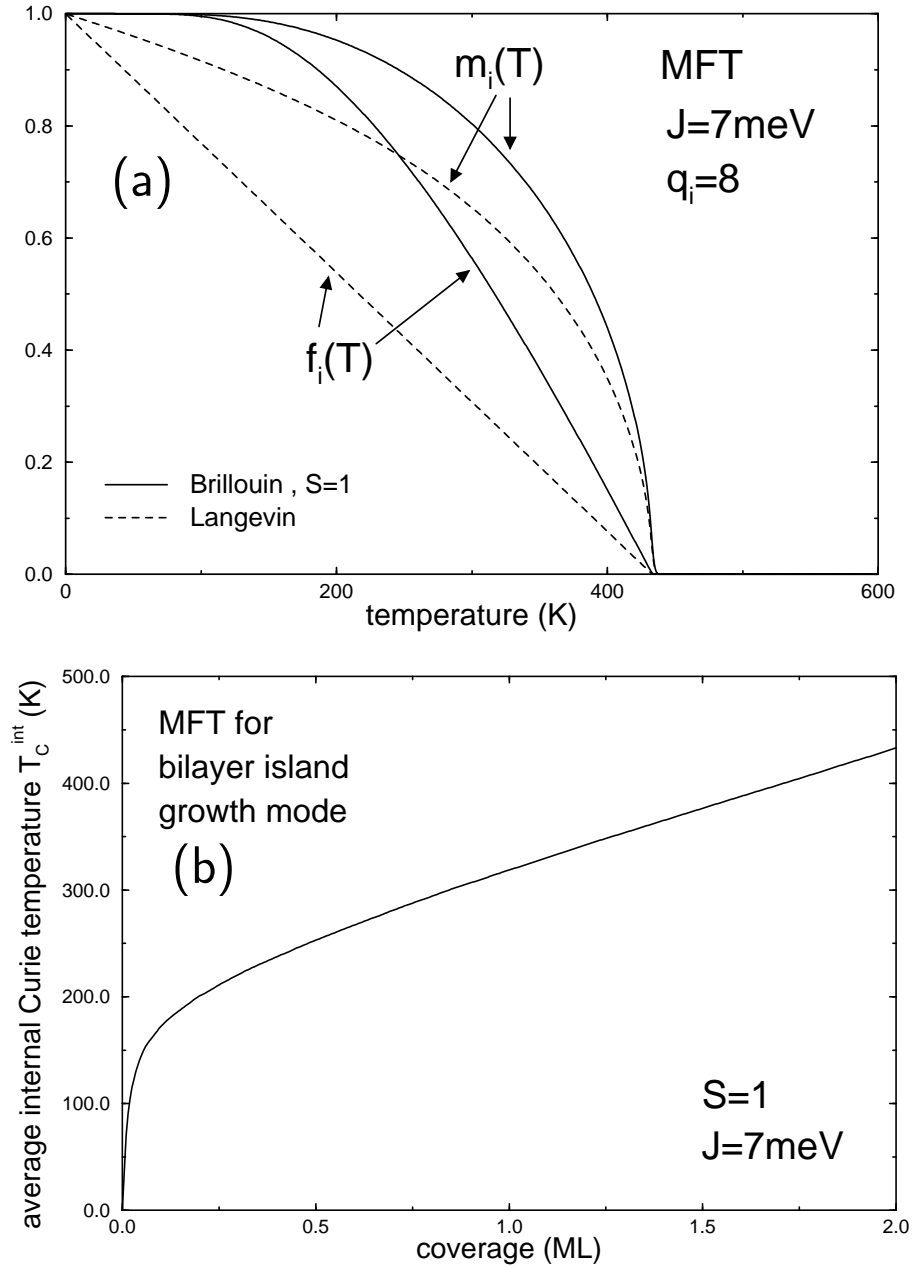
Figure F.1: Results from MFT for the internal island order. (a) Examples for the relative internal magnetization $m_i(T)$ and the relative anisotropy $f_i(T)$ of an island i are plotted versus the temperature T. The values $J = 7$ meV and $\overline{q}_i = 8$ were applied. Results for quantum spins, obtained by the Brillouin function for $S = 1$, and results for classical spins, obtained by the Langevin function, are shown. (b) The average internal Curie temperature $T_C^i(\Theta)$ for the bilayer island growth mode is plotted as function of the film coverage Θ. $S = 1$ quantum spins and $J = 7$ meV are assumed.

for $T \leq T_{\mathrm{C}}^i(\Theta)$ where $T_{\mathrm{C}}^i(\Theta)$ is given by Eq. (F.5).

Following the general derivation of the domain wall width, the influence of the finite temperature on the domain wall energy density between the islands is considered as [69, 77]

$$\gamma_{ij}(\Theta, T) = \gamma \sqrt{m_i(\Theta, T)\, m_j(\Theta, T)\, f_{ij}(\Theta, T)} \quad, \tag{F.11}$$

where $f_{ij}(\Theta, T)$ is the mean of $f_i(\Theta, T)$ and $f_j(\Theta, T)$ of islands i and j, see Eq. (F.7) or (F.10).

Fig. F.1 (a) shows examples for the internal island magnetization $m_i(T)$ and the relative anisotropy $f_i(T)$ as functions of the temperature T for $J = 7\,\mathrm{meV}$ and $\overline{q}_i = 8$. Results for $S = 1$ quantum spins and for classical spins are depicted; note that $m_i(T) \rightarrow 1$ and $f_i(T) \rightarrow 1$ for $T \rightarrow 0$. In Fig. F.1 (b), the average internal Curie temperature $T_{\mathrm{C}}^i(\Theta)$ is given as function of the film coverage Θ. The average coordination number $\overline{q}_i(\Theta)$ for the bilayer island growth mode, $S = 1$ quantum spins, and $J = 7\,\mathrm{meV}$ are applied to Eq. (F.3).

F.2 Long-range magnetic order

For a comparison with MC calculations, we derive a simple MFT for the *long-range* ordering of the nonuniform interacting island system at finite temperatures. We assume a two-state model $S_i = \pm 1$ for the island magnetization directions and use the corresponding Brillouin function.[2] The advantage of MFT comes from its simplicity compared to other methods, and from the fact that its qualitative predictions often agree well with experiments. However, MFT neglects fluctuation effects which destroy ordered phases for space dimensions less than the corresponding lower critical dimension.

Thermal agitation results in an effective reduction of the island spin $S_i \rightarrow \langle S_i \rangle$, with $-1 \leq \langle S_i \rangle \leq 1$, seen by the other islands. The island spin expectation values $\langle S_i \rangle$ are calculated by the self-consistent set of transcendental equations [153, 11, 133]

$$\langle S_i \rangle = \tanh\left(\tilde{H}_i / k_{\mathrm{B}} T\right) \quad, \quad i = 1, \ldots, Z \quad, \tag{F.12}$$

with Z the number of island spins in the system, and with the effective local field acting on island i

$$\tilde{H}_i = \tilde{H}_{\mathrm{dw}}^i + \tilde{H}_{\mathrm{dip}}^i \quad, \tag{F.13}$$

which results from the inter-island exchange and dipole couplings. From the micromagnetic model (Eq. (3.20)), the exchange term is given by

$$\tilde{H}_{\mathrm{dw}}^i = \sum_j L_{ij}\, \gamma_{ij}(\Theta, T)\, \langle S_j \rangle \quad. \tag{F.14}$$

---

[2]For vector island spins $\boldsymbol{S}_i$ with vanishing anisotropy, the Langevin function $\mathcal{L}(y) = \coth y - 1/y$ has to be used for the calculation of the expectation values $\langle \boldsymbol{S}_i \rangle$ [133].

The dipole interaction term reads either

$$\tilde{H}^i_{\mathrm{dip},1} = -\mu_i(\Theta, T) \sum_j \mu_j(\Theta, T) \, \langle S^z_j \rangle \left(\frac{x^2_{ij} + y^2_{ij}}{r^5_{ij}} \right) \quad , \qquad \text{(F.15)}$$

for out-of-plane island magnetizations, or

$$\tilde{H}^i_{\mathrm{dip},2} = -\mu_i(\Theta, T) \sum_j \mu_j(\Theta, T) \, \langle S^x_j \rangle \left(\frac{y^2_{ij} - 2x^2_{ij}}{r^5_{ij}} \right) \quad , \qquad \text{(F.16)}$$

for in-plane island magnetizations, depending on the chosen case for the easy axes.

The self-consistent set of equations can be solved numerically by a simple iterative method, where in the nth step of the iteration a set of island spin expectation values $\{\langle S_i \rangle^{(n)}\}$ is used to calculate a set of effective local fields $\{\tilde{H}^{(n)}_i\}$, from which a new set of spin variables $\{\langle S_i \rangle^{(n+1)}\}$ is generated. This scheme can be started with the saturated states $\langle S_i \rangle^{(1)} \equiv 1$ and is iterated, until convergence and the desired degree of accuracy is obtained. We note that using this method, minima of the free energy are found, not necessarily the global minimum.

From this solution, the overall magnetization M_{MFT} for a given film structure, which is a measure of the long-range order of the system, is calculated by

$$M_{\mathrm{MFT}}(\Theta, T) = \frac{\sum_i m_i(\Theta, T) \, N_i(\Theta) \, \langle S_i \rangle}{\sum_i N_i(\Theta)} \quad . \qquad \text{(F.17)}$$

Additionally, M_{MFT} has to be averaged over a large number G of different structural realizations of the unit cell, yielding

$$[M_{\mathrm{MFT}}]_{\mathrm{av}} = \frac{1}{G} \sum_{g=1}^{G} M^{(g)}_{\mathrm{MFT}} \quad . \qquad \text{(F.18)}$$

The temperature, at which $[M_{\mathrm{MFT}}]_{\mathrm{av}}$ vanishes, refers to the magnetic ordering temperature $T^{\mathrm{MFT}}_{\mathrm{C}}$.